日本原子力研究開発機構機関リポジトリ

Japan Atomic Energy Agency Institutional Repository

Title	Large-scale shell-model calculations for unnatural-parity high-spin states in neutron-rich Cr and Fe isotopes
Author(s)	Tomoaki Togashi, Noritaka Shimizu, Yutaka Utsuno, Takaharu Otsuka, and Michio Honma
Citation	Physical Review C, 91(2), 024320 (2015).
Text Version	Publisher
URL	http://jolissrch-inter.tokai-sc.jaea.go.jp/search/servlet/search?5049614
DOI	http://dx.doi.org/10.1103/PhysRevC.91.024320
Right	© American Physical Society

Japan Atomic Energy Agency

Large-scale shell-model calculations for unnatural-parity high-spin states in neutron-rich Cr and Fe isotopes

Tomoaki Togashi,[1,*] Noritaka Shimizu,[1] Yutaka Utsuno,[1,2] Takaharu Otsuka,[1,3,4] and Michio Honma[5]

[1]*Center for Nuclear Study, University of Tokyo, Hongo, Bunkyo-ku, Tokyo 113-0033, Japan*
[2]*Advanced Science Research Center, Japan Atomic Energy Agency, Tokai, Ibaraki 319-1195, Japan*
[3]*Department of Physics, University of Tokyo, Hongo, Bunkyo-ku, Tokyo 113-0033, Japan*
[4]*National Superconducting Cyclotron Laboratory, Michigan State University, East Lansing, Michigan, 48824, USA*
[5]*Center for Mathematical Sciences, University of Aizu, Ikki-machi, Aizu-Wakamatsu, Fukushima 965-8580, Japan*

We investigate unnatural-parity high-spin states in neutron-rich Cr and Fe isotopes using large-scale shell-model calculations. These shell-model calculations are carried out within the model space of fp-shell $+ 0g_{9/2} + 1d_{5/2}$ orbits with the truncation allowing $1\hbar\omega$ excitation of a neutron. The effective Hamiltonian consists of GXPF1Br for fp-shell orbits and V_{MU} with a modification for the other parts. The present shell-model calculations can describe and predict the energy levels of both natural- and unnatural-parity states up to the high-spin states in Cr and Fe isotopes with $N \leqslant 35$. The total energy surfaces present prolate deformations on the whole and indicate that the excitation of one neutron into the $0g_{9/2}$ orbit plays the role of enhancing prolate deformation. For positive (unnatural)-parity states in odd-mass Cr and Fe isotopes, their energy levels and prolate deformations indicate the decoupling limit of the particle-plus-rotor model. The sharp drop of the $9/2_1^+$ levels in going from $N = 29$ to $N = 35$ in odd-mass Cr, Fe, and Ni isotopes is explained by the Fermi surface approaching the $\nu 0g_{9/2}$ orbit.

I. INTRODUCTION

The evolution of the shell structure in neutron-rich nuclei is one of the main interests in modern nuclear physics. The neutron-rich fp-shell region has attracted particular attraction in this context because new neutron magic numbers have recently been established. The subshell closure at $N = 32$ is indicated by the high 2_1^+ levels and reduced $B(E2,0_1^+ \rightarrow 2_1^+)$ values in ^{52}Ca [1,2], ^{54}Ti [3,4], and ^{56}Cr [5,6] compared to neighboring isotopes. A new subshell closure at $N = 34$ was observed in ^{54}Ca in 2013 [7], more than a decade after its prediction [8]. Evaluating the evolution of these shell gaps is facilitated by advances in shell-model calculations for the full fp-shell space [9,10]. The appearance of the $N = 32$ and $N = 34$ magic numbers in the proton-deficient region is attributed to the tensor-force-driven shell evolution [11].

The evolution of the shell gap at $N = 40$, one of the main subjects of this paper, constitutes a key to understanding the characteristic features of the nuclear structure in the neutron-rich $N \sim 40$ region. While the $N = 40$ magicity seems to be rather stable in Ni isotopes [12–14], it breaks down completely in Cr and Fe isotopes: very low 2_1^+ levels and large $B(E2,0_1^+ \rightarrow 2_1^+)$ values in $^{60-64}$Cr [15–18] and $^{66-68}$Fe [15,18,19] cannot be reproduced without considerable neutron excitations across the $N = 40$ shell gap [20–22]. Most recently, it has been reported that the breakdown of the $N = 40$ magicity can possibly be extended even to Ti isotopes [23] having less proton-neutron quadrupole collectivity than the Cr and Fe isotopes. This abrupt nuclear-structure change from Ni to lower-Z isotopes is analogous to what is observed in the so-called "island of inversion" region around ^{32}Mg [24], where

neutron excitation induces a large deformation. The evolution of the $N = 40$ shell gap contributes greatly to the formation of the island of inversion in Cr and Fe isotopes. Indeed, it is suggested in Ref. [22] that the $N = 40$ shell gap decreases with a decreasing proton number in a similar way to the evolution of the $N = 20$ gap proposed in Ref. [25]. The tensor force accounts for this reduction in the harmonic-oscillator shell gaps at $N = 20$ and 40 toward a lower Z and, also, plays a crucial role in the occurrence of the spherical-oblate-prolate shape coexistence in ^{68}Ni through the type II shell evolution proposed in Ref. [26].

While the evolution of the $N = 40$ shell gap thus causes a number of intriguing phenomena, it is very difficult to directly deduce this shell gap from the structure of the Cr and Fe isotopes that belong to the island of inversion. This is because low-lying states of those nuclei are dominated by multiparticle multihole excitations, and this property is not very sensitive to small changes in the shell gap. On the other hand, states dominated by one-particle one-hole ($1p$-$1h$) excitation provide more direct information on the $N = 40$ shell gap, when these levels are compared to the $0p$-$0h$ states. For Cr and Fe isotopes, low-lying unnatural-parity states with $N \leqslant 35$ are regarded as such $1p$-$1h$ states because low-lying natural-parity states in this region are excellently described within the fp-shell configurations [9]. The nuclear properties of unnatural-parity states in Cr and Fe isotopes in the last decade have been measured mainly from γ-ray spectroscopy experiments. Important findings of recent experiments include a sharp drop in $9/2_1^+$ levels upon going from $N = 29$ to $N = 35$ observed in Cr and Fe isotopes [27–31]. If this change in energy level is an indication of a sharp evolution of the $0g_{9/2}$ orbit with increasing neutron number as suggested in Ref. [20], the driving force of the evolution needs to be clarified.

---

*togashi@cns.s.u-tokyo.ac.jp

Another significant nuclear-structure issue in the unnatural-parity states in Cr and Fe isotopes is their nuclear shapes; in particular, how these shapes are polarized by an additional neutron in the $0g_{9/2}$ orbit. The development of deformation is indicated experimentally by the regular spacing between $\Delta I = 2$ energy levels observed up to high-spin states [27,28,30–32]. While various models show the dominance of prolate deformation in the ground states of Cr isotopes (see [33], for instance), an oblate deformation in the unnatural-parity band of ^{59}Cr was suggested in Ref. [29] from the observed isomeric $9/2^+$ state located at 503 keV, which should be the lowest among the unnatural-parity states. This level is interpreted naively as the bandhead of the $K = 9/2$ intrinsic state, which appears to be the lowest for oblate deformation. On the other hand, a recent study with a projected shell-model calculation has shown that prolate deformation is favored based on comparison with experimental data [34]. A similar isomeric $9/2^+$ state is observed in ^{61}Fe, and its magnetic moment [35] and absolute value of quadrupole moment [36] support prolate deformation according to the particle-triaxial-rotor model [31]. More elaborate systematic calculations incorporating various degrees of freedom for deformation and configuration help draw a definite conclusion about the shape evolution in Cr and Fe isotopes.

In this paper, we report systematic large-scale shell-model calculations for natural-parity and unnatural-parity states in Cr and Fe isotopes for $N \leqslant 35$, by clarifying the structure of their $0p$-$0h$ and $1p$-$1h$ bands. Using a combination of known effective interactions that are slightly modified, we achieve excellent agreement with experiment in the whole region studied. This highly descriptive power enables extraction of shell and shape evolutions in this region. This paper is organized as follows. In Sec. II, we present our theoretical framework including the effective Hamiltonian used in this work. In Sec. III, first, we show the results of the energy levels for neutron-rich Cr and Fe isotopes, and second, we discuss the deformation for the natural- and unnatural-parity states in these nuclei. In Sec. IV, we discuss how the $\nu 0g_{9/2}$ orbit evolves in this mass region by using theoretical and experimental information. Conclusions of this study are presented in Sec. V.

II. THEORETICAL FRAMEWORK

A. Shell-model calculation

In the mass region of Z or N from 20 to 40, natural-parity states with $\pi = +(-)$ for even (odd)-mass nuclei are usually described well within the fp-shell model space with a ^{40}Ca inert core. However, unnatural-parity states with $\pi = -(+)$ for even (odd)-mass nuclei cannot be described within one major fp shell. In the quasi-SU3 model [37], the pairs of $\Delta j = 2$ orbits of a major shell describe the quadrupole collectivity. Hence, we choose the $0g_{9/2}$ and $1d_{5/2}$ orbits and add them to the fp-shell model space. In the present shell-model calculation, the model space is composed of fp-shell $(0f_{7/2}, 0f_{5/2}, 1p_{3/2}, 1p_{1/2}) + 0g_{9/2} + 1d_{5/2}$ orbits. To focus on the states dominated by $1p$-$1h$ excitation across the $N = 40$ shell gap, a truncation is introduced so that one neutron is

allowed to occupy the $0g_{9/2}$ or $1d_{5/2}$ orbit, which means that the $1\hbar\omega$ excitation of a neutron to the gds shell occurs only in unnatural-parity states.

The present shell-model Hamiltonian has the following form, which consists of one- and two-body terms,

$$H = \sum_i \varepsilon_i c_i^\dagger c_i + \sum_{i<j,k<l} V_{ijkl}\, c_i^\dagger c_j^\dagger c_l c_k + \beta_{\text{c.m.}} H_{\text{c.m.}}, \quad (1)$$

where ε_i and V_{ijkl} represent the bare single-particle energy and the two-body matrix element, respectively, $c_i^\dagger$ (c_i) denotes a creation (annihilation) operator of a nucleon in a single-particle orbit i, and $\beta_{\text{c.m.}} H_{\text{c.m.}}$ is the term proposed by Gloeckner and Lawson to remove the spurious center-of-mass motion due to the excitation beyond one major shell [38]. The parameter of $\beta_{\text{c.m.}}$ is applied as $\beta_{\text{c.m.}} \hbar\omega / A = 10$ MeV, where A is the mass number: $A = Z + N$. We take $\hbar\omega$ from the empirical value: $\hbar\omega = 41.0 A^{-1/3}$ MeV.

In the present work, the Hamiltonian matrix with an M scheme is diagonalized by the thick-restart Lanczos method with the MSHELL64 code [39] for a dimension of the matrix below 10^9 and the KSHELL code [40] for a dimension over 10^9.

B. The effective Hamiltonian

In this subsection, we explain the details of the effective Hamiltonian in Eq. (1) in the present work. For shell-model calculations within the fp-shell model space, the GXPF1A Hamiltonian [41] is often applied to reproduce and to predict the properties of nuclei in the region of Z or N from 20 to 40. Recently, the GXPF1A Hamiltonian has been improved to explain the observed energy levels in neutron-rich Ca isotopes: GXPF1B [42], with the modification of five $T = 1$ two-body matrix elements and the bare single-particle energy which involve the $1p_{1/2}$ orbit from GXPF1A; and GXPF1Br [7], with the modification of the monopole interaction for $\langle 0f_{5/2}1p_{3/2}|V|0f_{5/2}1p_{3/2}\rangle_{T=1}$ from GXPF1B. The GXPF1B Hamiltonian can reproduce the energy levels of ^{51,52}Ca, and the GXPF1Br Hamiltonian can reproduce those of ^{53,54}Ca besides ^{51,52}Ca. Here, we adopt the newest effective Hamiltonian, GXPF1Br, for fp-shell orbits. For neutron $1\hbar\omega$ excitation to the $0g_{9/2}$ or $1d_{5/2}$ orbits, we create the cross-shell two-body interaction between the fp-shell and the gds-shell orbits from V_{MU} [43]. V_{MU} has the central force of a simple Gaussian form and the $\pi + \rho$ mesons exchange tensor force, and reproduces the monopole properties of the shell-model Hamiltonian in sd and fp shells. We utilize V_{MU} with the refinement [44] by adding the M3Y spin-orbit force [45] and the density dependence for the central force described in Ref. [46]. All two-body matrix elements are scaled by $(A/42)^{-0.3}$ as the mass dependence.

In addition to the cross-shell two-body interaction, the bare single-particle energies with a ^{40}Ca inert core for the $0g_{9/2}$ and $1d_{5/2}$ orbits need to be determined. The bare single-particle energy of $0g_{9/2}$ is determined so as to reproduce the excitation energy of $9/2_1^+$ states systematically. However, determining the bare single-particle energy of $1d_{5/2}$ is more difficult than that of $0g_{9/2}$. The single-particle property of the $1d_{5/2}$ orbit in this mass region is masked. In fact, the experimental
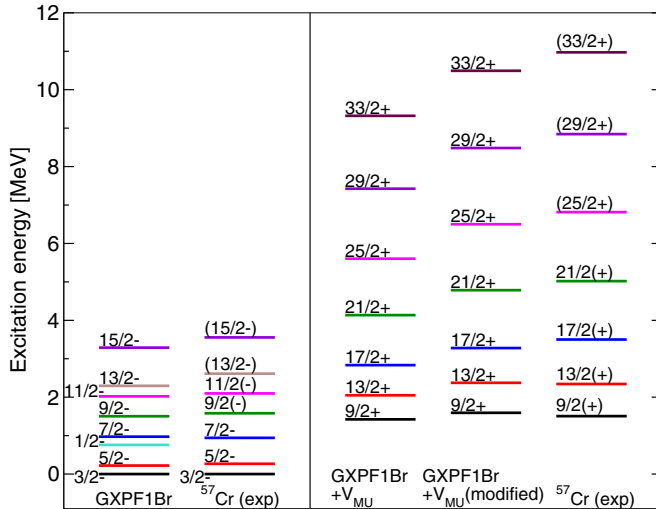
FIG. 1. (Color online) Shell-model results and experimental data on the energy levels of ^{57}Cr. Experimental data, labeled "^{57}Cr(exp)," are taken from [28].

spectroscopic factors of the $5/2_1^+$ state in neutron-rich odd-mass Cr and Fe nuclei are rather small in comparison with those of the $9/2_1^+$ state [47–49]. Here, we assume that the bare single-particle energy of $1d_{5/2}$ is equal to that of $0g_{9/2}$. This assumption is considered to be reasonable because the splitting of the effective single-particle energies (ESPEs) between $0g_{9/2}$ and $1d_{5/2}$ for nuclei taken in this study, around 2 MeV, is close to the phenomenological gds-shell orbits splitting in this mass region [50]. In the present work, the bare single-particle energy of $0g_{9/2}$ (=that of $1d_{5/2}$) is determined so as to be fitted to reproduce the excitation energies of $9/2_1^+$ in ^{55,57,59}Cr. The resulting value is 0.793 MeV.

Figure 1 shows the energy levels of ^{57}Cr and the results of the shell-model calculations with the above-mentioned Hamiltonian. As shown in Fig. 1, the fp shell-model calculation with GXPF1Br reproduces the negative(natural)-parity states quite well, and that with GXPF1Br + V_{MU} without modification reproduces the positive(unnatural)-parity states reasonably well. For further improvement, we change the cross-shell two-body matrix elements by -1.0 MeV for $\langle 0g_{9/2}0f_{5/2}|V|0g_{9/2}0f_{5/2}\rangle_{J=2,3,T=1}$ and by $+1.0$ MeV for $\langle 0g_{9/2}0f_{5/2}|V|0g_{9/2}0f_{5/2}\rangle_{J=6,7,T=1}$. This modification increases the energy intervals in the positive-parity band by about 15% as a whole. These results, labeled GXPF1Br + V_{MU}(modified) in Fig. 1, agree with the experimental data within ∼500 keV. In the following, we present the results for Cr and Fe isotopes with the new effective Hamiltonian, GXPF1Br + V_{MU}(modified).

III. RESULTS AND DISCUSSION

A. Energy levels

The results of the present shell-model calculation with GXPF1Br + V_{MU}(modified) are compared with the experimental data for Cr and Fe isotopes. We focus here on the lowest states for a given spin I and parity $\pi = \pm$. The results

for odd-mass and even-mass nuclei are shown in Figs. 2 and 3, respectively, where the unnatural-parity states are classified into two $\Delta I = 2$ sequences.

For the odd-mass $^{55-59}$Cr and $^{57-61}$Fe, as shown in Fig. 2, the negative-parity states are described well by the shell-model calculation within the fp-shell model space. Furthermore, almost all of the observed positive-parity states are reproduced excellently by the present shell-model calculation. For the highest-spin $37/2_1^+$ state in ^{57}Cr, the backbending indicated by the small energy interval between $37/2_1^+$ and $33/2_1^+$ [51] is not well reproduced in this calculation. This shows the limitation of description within the present model space and truncation. The theoretical results show that the $1/2_1^+$ and $5/2_1^+$ states lie at a higher energy than the $9/2_1^+$ state in each nucleus. This means that each $9/2_1^+$ state is the lowest state in its band. Actually, the $9/2_1^+$ and $5/2_1^+$ states observed in ^{55}Cr and ^{57,59}Fe are almost degenerate. The present shell-model calculation predicts that the other positive-parity band including $7/2_1^+$, $11/2_1^+$, ... is located higher than $13/2_1^+$ in each nucleus.

For even-mass ^{56,58}Cr and ^{58,60}Fe, as shown in Fig. 3, the present calculation excellently describes the positive- and negative-parity states except for some of the high-spin states and the 3_1^- states. The observed 3_1^- states lie at slightly lower energies than the calculated ones, which may indicate that these 3_1^- states are described not as a single particle-hole configuration but as collective states, for instance, octupole vibrational states. The relative positions of the negative-parity odd-I and even-I bands are well reproduced with the present calculation. In ^{58}Fe, for instance, the 6_1^- and 8_1^- levels are located higher than the 7_1^- and 9_1^- levels, respectively, whereas higher-spin states follow the regular ordering according to spin. In contrast, we predict that the $\Delta I = 1$ partners such as 6_1^- and 7_1^- lie very close to high-spin states for ^{56}Cr.

One of the interesting features of these Cr and Fe nuclei is that the level spacing between $\Delta I = 2$ of the band built on $9/2_1^+$ in the odd-mass A nuclei is similar to that of the 0_1^+ band in the neighboring even-mass $A - 1$ nuclei. For $^{56-59}$Cr, in Fig. 4, we compare the level spacing of the positive-parity yrast states between even- and odd-mass nuclei, which has already been discussed for ^{54,55}Cr [27] and $^{56-61}$Fe [31]. One can see the similar level spacing between the yrast band in even-mass nuclei and the band of the $9/2_1^+$ in odd-mass nuclei. Although the experimental information for the high-spin states in ^{59}Cr is not enough, the present calculation predicts this similarity of the level spacing between $^{58-59}$Cr. This level structure indicates the decoupling limit of the particle-plus-rotor model [57,58] as discussed in the next subsection.

B. Deformations

In this subsection, we discuss the deformations for natural- and unnatural-parity states in neutron-rich Cr and Fe nuclei in terms of their intrinsic quadrupole moments. There is no straightforward way to determine the intrinsic quadrupole moments with the shell-model calculations because the shell-model wave functions are described in the laboratory frame. Here we probe deformations from two approaches. One is approximating the wave function in the intrinsic frame. The
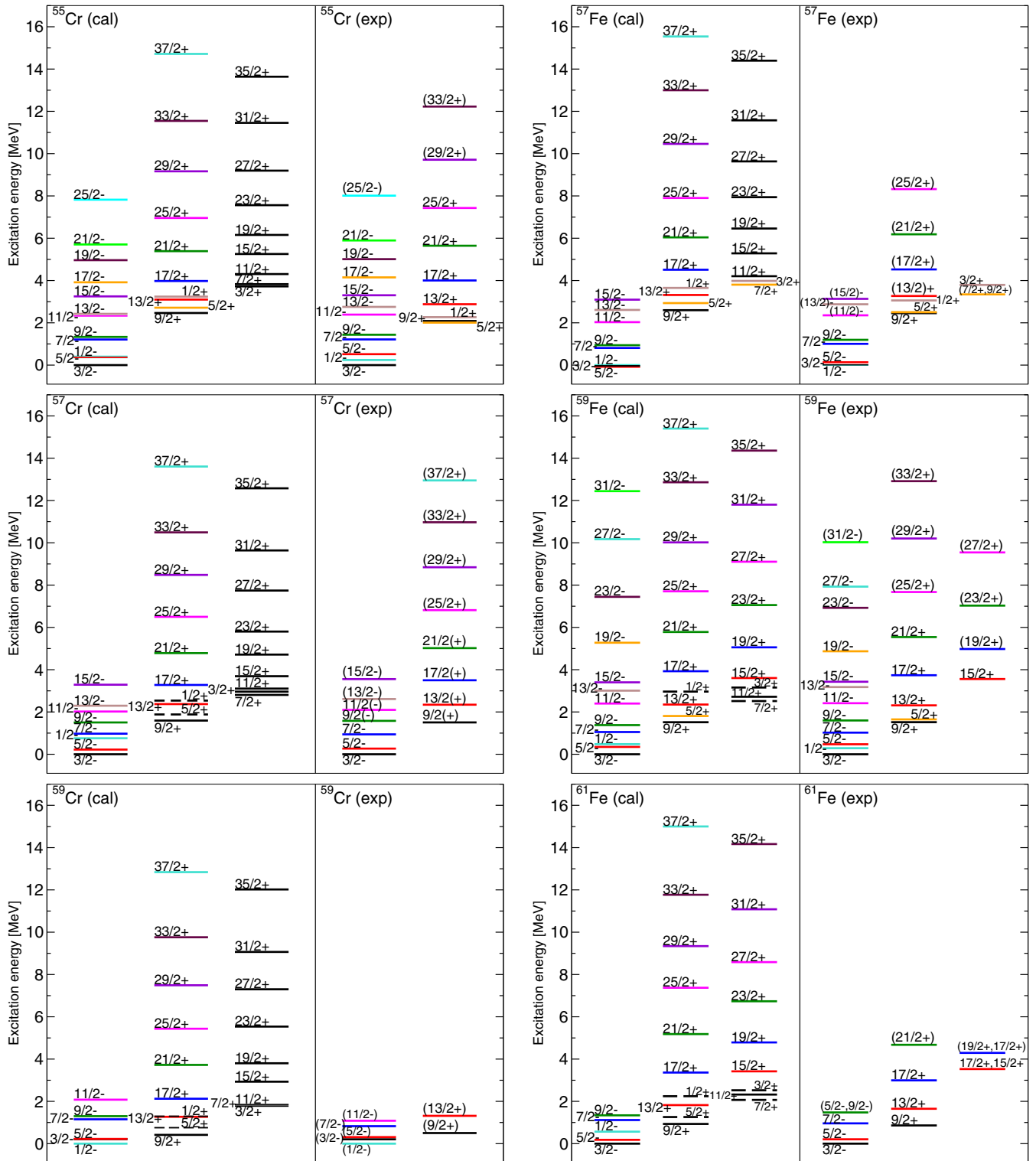
FIG. 2. (Color online) Calculated and experimental energy levels of the lowest states for each spin and parity in odd-mass Cr and Fe isotopes. In each plot, the left and right panels present the calculated and experimental energy levels, respectively. Experimental data are taken from [28–32,47–49,51].

other is extracting intrinsic deformations from shell-model wave functions using the geometric model.

The intrinsic-frame approximation in the shell model is often performed with the Q-constrained Hartree-Fock method

[59,60]. This method is, however, not suitable for deducing intrinsic wave functions for unnatural-parity states, which are usually located higher than natural-parity states. In the present study, we calculate the total energy surfaces separately
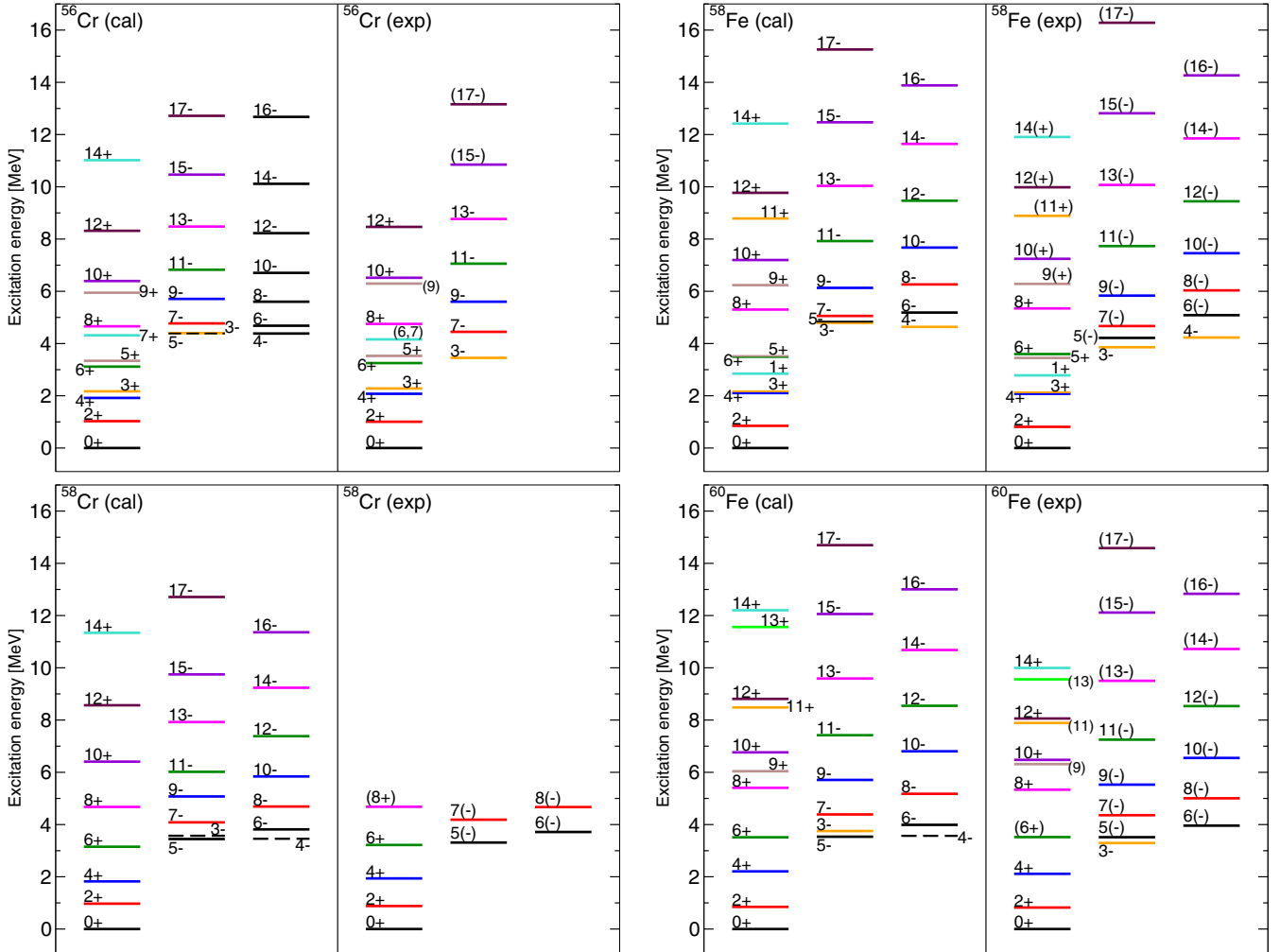
FIG. 3. (Color online) Calculated and experimental energy levels of the lowest states for each spin and parity in even-mass Cr and Fe isotopes. The notation is the same as in Fig. 2. Experimental data are taken from [30,51–55]. In ^{58}Fe, experimental negative-parity states, except for the 3^-_1 and 4^-_1 states, are taken from bands 2 and 3 in Ref. [52], where these states are discussed based on the projected shell-model calculation [56] interpreting them as negative-parity states.

for positive- and negative-parity states by performing the Q-constrained Hartree-Fock calculation with variation after parity projection. We utilize the parity-projected wave function $|\Phi^\pi\rangle$ written as

$$|\Phi^\pi\rangle = \frac{1 + \pi\Pi}{2}|\Phi\rangle, \quad |\Phi\rangle = \prod_i^{N_f}\left(\sum_l^{N_s} D_{li}\, c_l^\dagger\right)|-\rangle, \quad (2)$$

where Π represents the space-reflection operator, π denotes the parity, $\pi = \pm$, N_f and N_s represent the numbers of the valence particles and the single-particle orbits in the model space, respectively, and $|-\rangle$ denotes an inert core. The coefficients D in $|\Phi\rangle$ of Eq. (2) are determined to minimize the energy $\langle\Phi^\pi|H|\Phi^\pi\rangle/\langle\Phi^\pi|\Phi^\pi\rangle$ with the constraints of quadrupole moments $\langle Q_0\rangle = \langle\Phi^\pi|Q_0|\Phi^\pi\rangle/\langle\Phi^\pi|\Phi^\pi\rangle$ and $\langle Q_2\rangle = \langle\Phi^\pi|Q_2|\Phi^\pi\rangle/\langle\Phi^\pi|\Phi^\pi\rangle$, where the intrinsic axes are chosen to satisfy $\langle\Phi^\pi|Q_{\pm1}|\Phi^\pi\rangle = 0$. Q_μ is the μ component of the mass quadrupole operator. Note that the wave function of Eq. (2) is solved by using the shell-model Hamiltonian.

The total energy surfaces for the negative- and positive-parity states in odd-mass $^{55-59}$Cr and $^{57-61}$Fe are shown in Fig. 5. These energy surfaces indicate the dominance of prolate deformation. For negative-parity states, the quadrupole moments at the energy minima are around 100 fm^2. For positive-parity states, these values are enlarged to be around 120 fm^2. The wave functions near the energy minima of the positive-parity energy surfaces are dominated by the excitation of one neutron into the $0g_{9/2}$ orbit. This confirms the validity of the truncation of the model space introduced in this study. While the one-neutron excitation into the $0g_{9/2}$ orbit induces larger deformation, by $\sim$20%, the shape is not changed significantly. In ^{59}Cr, the energy surfaces are γ-soft for both negative- and positive-parity states. In ^{61}Fe, γ-softness is seen for the positive-parity state. For the positive-parity state of ^{59}Fe, triaxiality is well developed.

The situation of the even-mass Cr and Fe nuclei is very similar to that of the odd-mass nuclei as shown in Fig. 6. These
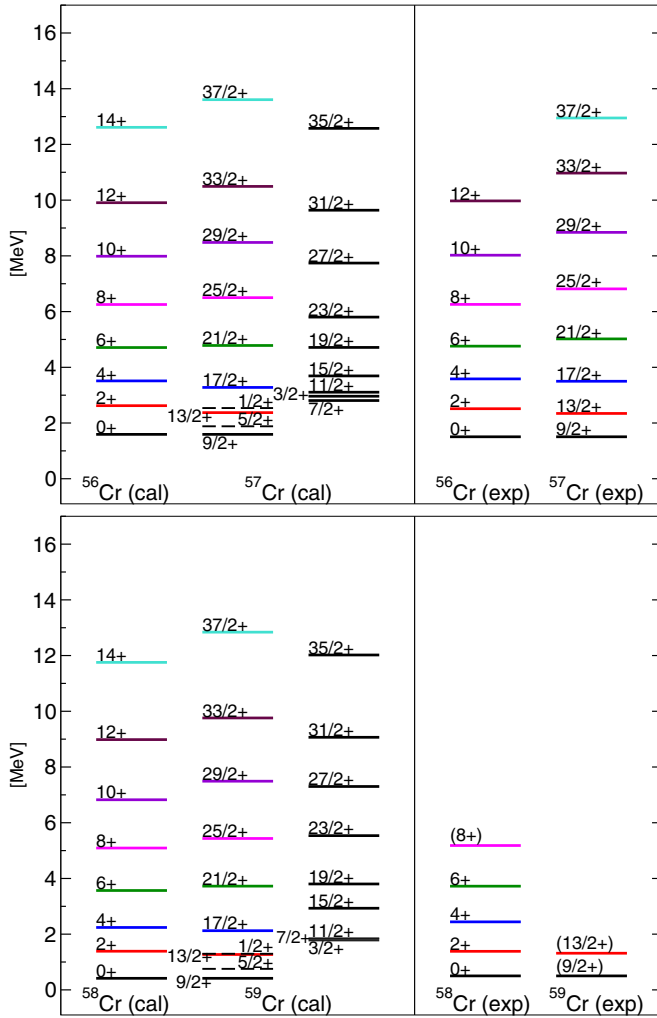
FIG. 4. (Color online) Comparison of the level spacing of the yrast bands in ^{56,58}Cr versus the bands built on $9/2_1^+$ in ^{57,59}Cr.

energy surfaces indicate the dominance of prolate deformation. For negative-parity states in even-mass nuclei, larger prolate deformations are induced by the excitation of one neutron into the $\nu 0g_{9/2}$ orbit. In ^{58}Fe, triaxiality is developed for both positive- and negative-parity states as suggested by the γ-vibrational band [52,61]. In ^{60}Fe, triaxiality is developed for the negative-parity state.

The intrinsic quadrupole moment Q_0 can also be deduced from the spectroscopic quadrupole moment Q_S by assuming the K quantum number [50] as

$$Q_S = \frac{3K^2 - I(I+1)}{(I+1)(2I+3)} Q_0, \quad (3)$$

where I denotes the spin of the state. Q_S is an observable and is also calculated directly by the shell model. We calculate Q_S with the effective charges $e_\pi = 1.5e$ and $e_\nu = 0.5e$. The results for the band members starting from $9/2_1^+$ are shown in Fig. 7, together with the experimental data for the $9/2_1^+$ state in ^{61}Fe [36]. The calculation reasonably reproduces the measured value. It should be noted that the magnetic moment of this state, $-1.031(9)\mu_N$ [35], is also close to

the calculated value, $-0.934\mu_N$, using the free-nucleon g factors.

Since Q_0 is identical among the members of an ideal rotor, the stability of Q_0 within a band provides a key to determining the intrinsic state. Here, we take the two possibilities of K for the band members built on $9/2_1^+$: $K = 1/2$ and $9/2$ correspond to prolate and oblate shapes, respectively. Figure 7 shows the intrinsic quadrupole moment Q_0 assuming $K = 1/2$ for odd-mass nuclei $^{55-59}$Cr and $^{57-61}$Fe. As shown in Fig. 7, the Q_0 value is nearly constant in Cr isotopes, whereas it decreases for high-spin states in Fe isotopes. This decrease might be due to a change in shape or K number, as suggested by the predicted backbending in the $29/2_1^+$ of ^{61}Fe (see Fig. 2). If $K = 9/2$ is assumed, on the other hand, we find a singular behavior of the Q_0 value for each nucleus: the Q_0 value is about $-600 \, e \, \text{fm}^2$ in the $13/2_1^+$ state and it suddenly transits into the large positive value of about $600 \, e \, \text{fm}^2$ in the $17/2_1^+$ state.

The intrinsic quadrupole moment Q_0 is also connected to the $B(E2, I \rightarrow I - 2)$ value [50],

$$B(E2, I \rightarrow I - 2) = \frac{5}{16\pi} (\langle I K 20 | I - 2 \, K \rangle)^2 \, Q_0^2, \quad (4)$$

where $\langle I K 20 | I - 2 \, K \rangle$ denotes the Clebsch-Gordan coefficient. Note that the sign of Q_0 cannot be determined using Eq. (4). We calculate the $B(E2)$ values with the same effective charges as used for Q_S. The bottom panels in Fig. 7 show the absolute values of Q_0 solved by Eq. (4) under the assumptions of $K = 1/2$ and $K = 9/2$. The present calculation reproduces the experimental $B(E2, 13/2_1^+ \rightarrow 9/2_1^+)$ in ^{59}Fe. Similarly to Q_S, the $B(E2)$ values lead to much more stable intrinsic quadrupole moments with $K = 1/2$ than with $K = 9/2$. Although the mixing of the K quantum numbers occurs in reality due to the Coriolis effect, the present calculation supports the dominance of $K = 1/2$ rather than $K = 9/2$ and thus prolate deformation for the odd-mass Cr and Fe nuclei studied.

We point out here that the overall prolate deformation in the positive-parity states of ^{55,57,59}Cr and ^{57,59,61}Fe is indeed suggested by the measured energy levels, according to the analysis of the particle-plus-rotor model presented in Refs. [57,58]. It is quite reasonable to apply the particle-plus-rotor model in which the last neutron occupies the $j = 9/2$ orbit because the $9/2_1^+$ states of these nuclei have rather large $\nu 0g_{9/2}$ spectroscopic factors as presented in the next section. The level structure realized by the particle-plus-rotor model strongly depends on the strength of the Coriolis term relative to the Ω^2 term (originating from the Nilsson levels and recoil term), where Ω is the projection of the angular momentum j of an orbit onto the symmetry axis. We here consider the case where the j orbit is occupied by the last nucleon alone. For oblate deformation having the maximum $\Omega (=j)$, the Coriolis term is less dominant because its matrix element is proportional to $(j(j+1) - \Omega^2)^{1/2}$. The energy levels then follow the strong-coupling limit of $I(I+1)/2\mathcal{I}$ ($I = \Omega, \Omega + 1, \Omega + 2, \ldots$), where $\mathcal{I}$ is the moment of inertia. For prolate deformation, on the other hand, the Coriolis term can dominate the Ω^2 term, especially when a high-j orbit is involved. The energy levels in this case follow the decoupling limit of $(I - \alpha)(I - \alpha + 1)/2\mathcal{I}$, where α is the
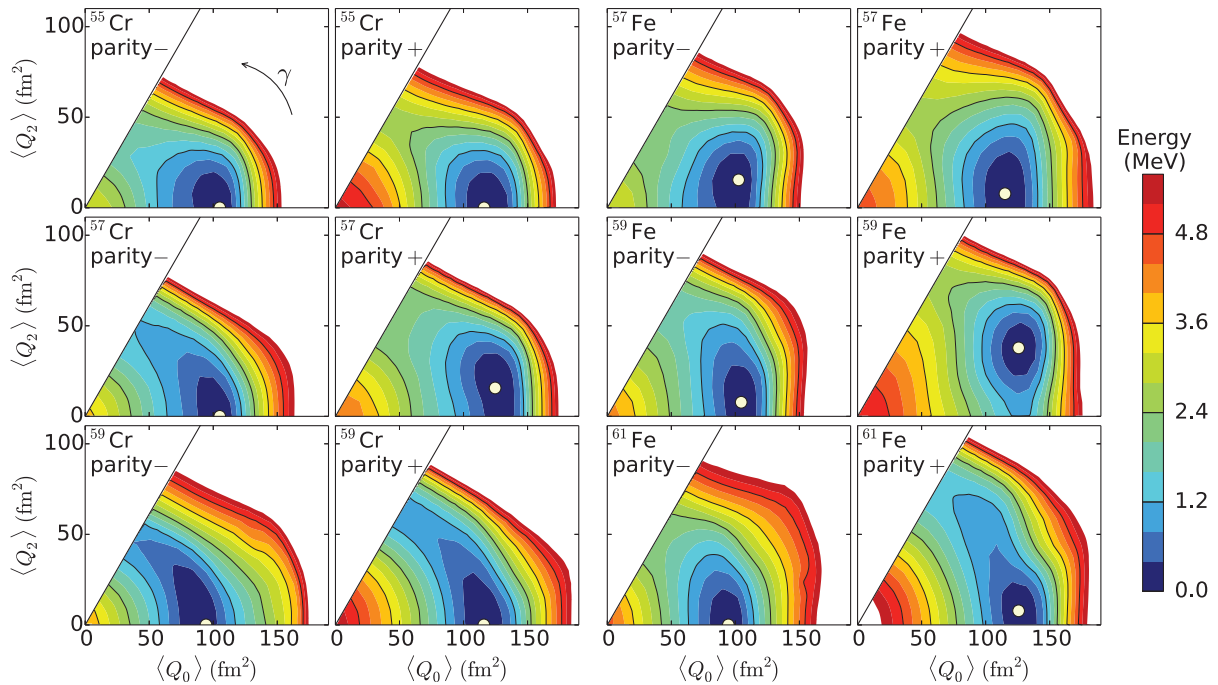
FIG. 5. (Color online) Total energy surfaces for the negative (natural)- and positive (unnatural)-parity states in odd-mass nuclei. Energy minima are represented by white circles. Energy contours are based on the energy minima starting from 0 MeV.

projection of j onto the rotation axis. The lowest-lying states take the largest possible α. Since symmetry considerations require $I - \alpha$ to be even, favored states with $\alpha = j$ consist of $I = j, j + 2, j + 4, \ldots$ and unfavored states with $\alpha = j - 1$ consist of $I = j + 1, j + 3, j + 5, \ldots$. As a result, two major differences arise between prolate and oblate shapes. One is that the splitting of the favored and unfavored states is seen only for prolate deformation. The other is that energy spacings in the $I = j, j + 2, j + 4, \ldots$ levels are identical to those of the even-even core, $0^+, 2^+, 4^+, \ldots$, for prolate deformation but are much wider for oblate deformation. Those differences are also obtained from a microscopic calculation using the projected shell model [34]. The observed levels shown in

Figs. 2 and 4 clearly support the decoupling limit which is realized for prolate deformation. Oblate deformation is quite unlikely but might not be completely excluded if deformation is small. Measuring unfavored states will provide additional information on shape.

IV. EVOLUTION OF THE $\nu 0g_{9/2}$ ORBIT

In this section, we examine what causes the sharp drop in the $9/2_1^+$ level with increasing neutron number observed in Cr and Fe isotopes. A particular attention is paid to the relation to the evolution of the $\nu 0g_{9/2}$ orbit. For this purpose, we also investigate the $9/2_1^+$ levels in Ni isotopes, which should more
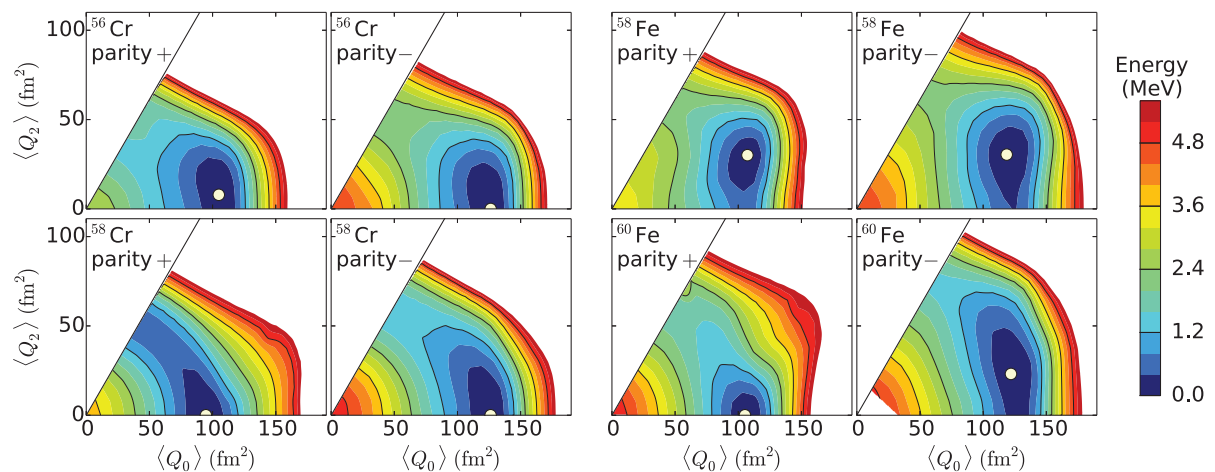

FIG. 6. (Color online) Total energy surfaces for positive(natural)- and negative(unnatural)-parity states in even-mass nuclei. Notation is the same as in Fig. 5.
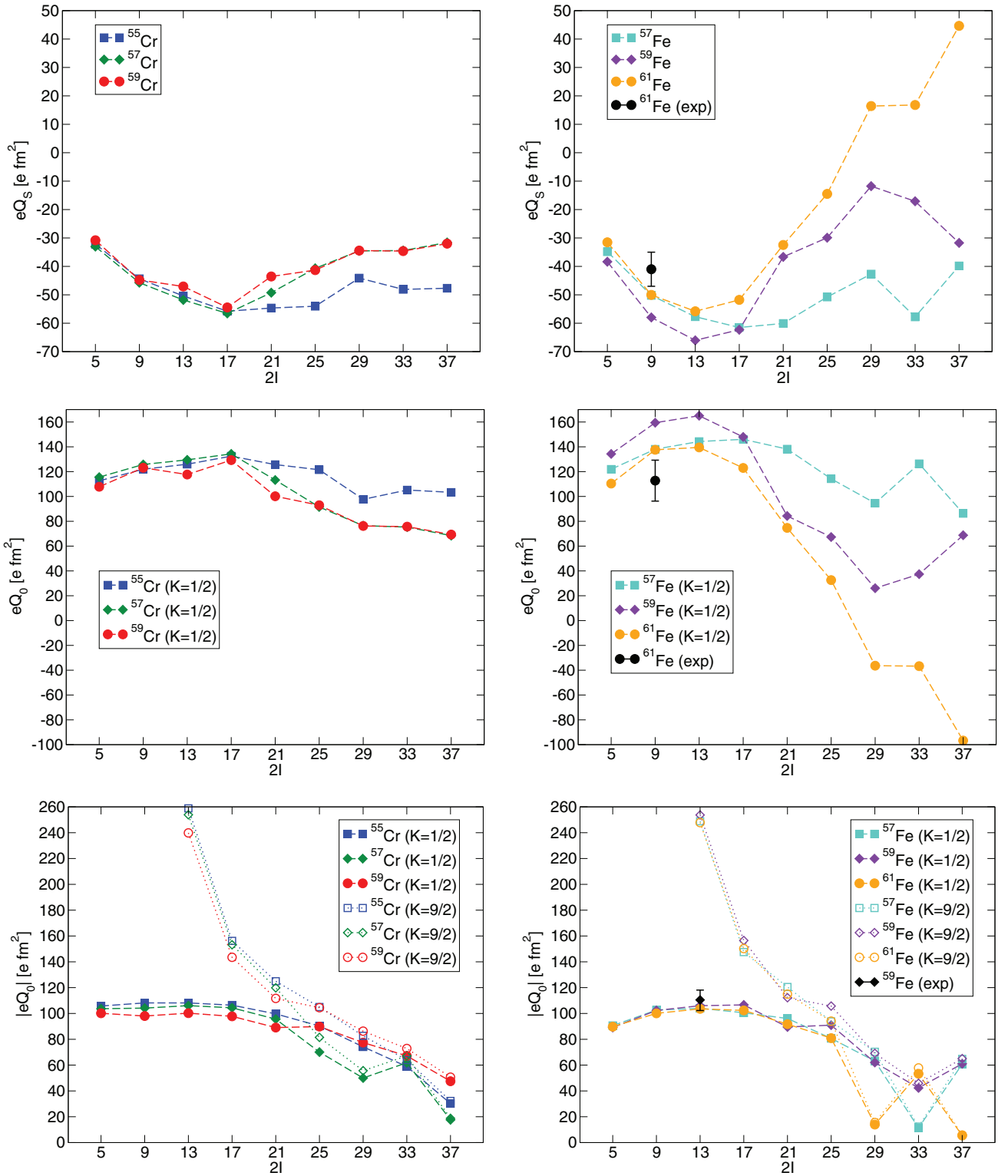
FIG. 7. (Color online) Electric spectroscopic and intrinsic quadrupole moments for members of the band built on $9/2_1^+$ in odd-mass Cr and Fe nuclei. Horizontal axes denote the spin I values of the states as $2I$. Upper panels show the electric spectroscopic quadrupole moments Q_S. Middle and lower panels show the intrinsic quadrupole moments Q_0 solved by Eq. (3) assuming $K = 1/2$ and the absolute values of Q_0 solved by Eq. (4), respectively. The experimental spectroscopic quadrupole moment Q_S of ^{61}Fe [36] labeled "^{61}Fe(exp)" is assumed to be negative. The absolute value of Q_0 labeled "^{59}Fe(exp)" is evaluated with the experimental $B(E2)$ values [49] assuming $K = 1/2$.
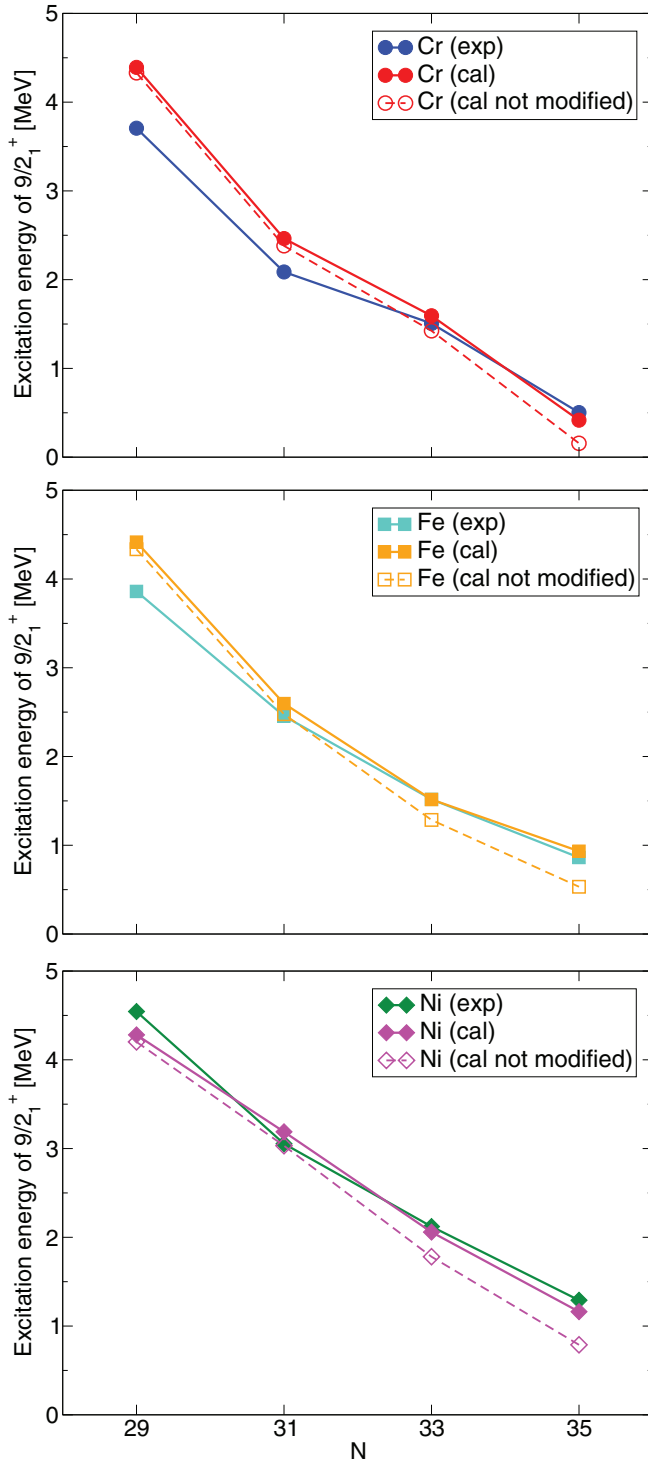
FIG. 8. (Color online) Excitation energy of $9/2_1^+$ in odd-mass Cr, Fe, and Ni isotopes from $N = 29$ to $N = 35$. Plots labeled "cal" and "exp" represent the present results and the experimental data, respectively. Plots labeled "cal not modified" show the results without modification of the two-body matrix elements described in Sec. II B. Experimental data are taken from [27–31,47–49,62–64]. In ^{55}Fe, the state of 3.86-MeV excitation energy in Ref. [47] is adopted as the experimental $9/2^+$ state because it has the largest spectroscopic factor of $9/2^+$ in the (d, p) reaction.

TABLE I. Spectroscopic factors of $\nu 0g_{9/2}$ and $\nu 1d_{5/2}$ particle states for $9/2_1^+$ and $5/2_1^+$, respectively. Experimental values (Exp) are taken from the data on the (d, p) reaction [65–84], the $(\alpha, {}^3{\rm He})$ reaction [85], the $({}^7{\rm Li}, {}^6{\rm Li})$ reaction [86], and the $({}^{14}{\rm C}, {}^{13}{\rm C})$ reaction [87]. Experimental excitation energies of $5/2^+$ in ^{53}Cr and ^{55}Fe are 4.13 and 4.46 MeV, respectively. Calculated (Cal) excitation energies of $5/2_1^+$ are 5.09 and 5.19 MeV for ^{53}Cr and ^{55}Fe, respectively.

	Cal	Exp
		$C^2S\,(9/2_1^+)$
^{53}Cr	0.564	0.520 [65], 0.95 [66], 0.57 [67]
^{55}Cr	0.458	0.67 [66], 0.582 [68]
^{57}Cr	0.479	–
^{59}Cr	0.498	–
^{55}Fe	0.568	0.74 [69], 0.465 [70], 0.375 [85], 0.67 [86]
^{57}Fe	0.494	0.270 [71], 0.447 [72]
^{59}Fe	0.442	0.510 [73], 0.38 [74]
^{61}Fe	0.527	–
^{57}Ni	0.611	–
^{59}Ni	0.580	0.84 [75], 0.47 [76], 0.56 [74], 0.381 [77], 0.390 [85], 0.69 [87]
^{61}Ni	0.503	0.62 [78], 0.750 [79], 0.8450 [80], 0.537 [81]
^{63}Ni	0.446	0.61 [69], 0.672 [82], 0.75 [83], 0.75 [84]
		$C^2S\,(5/2_1^+)$
^{53}Cr	0.161	0.090 [65], 0.13 [66], 0.10 [67]
^{55}Cr	0.142	0.225 [66], 0.145 [68], 0.17 [74]
^{57}Cr	0.148	–
^{59}Cr	0.152	–
^{55}Fe	0.117	0.172 [69], 0.079 [70], 0.13 [67], 0.25 [86]
^{57}Fe	0.120	0.110 [71], 0.114 [72]
^{59}Fe	0.113	0.128 [73], 0.11 [74]
^{61}Fe	0.133	–

directly reflect the spherical single-particle structure. It is noted that the maximum M-scheme dimension reaches 1.8×10^{10} for ^{59}Ni.

We first confirm the descriptive power of our approach. Figure 8 shows the results of the excitation energy of $9/2_1^+$ from $N = 29$ to $N = 35$. The sharp drop in $9/2_1^+$ is reproduced quite well in the present calculations. Although the evolution of the $9/2_1^+$ level is improved, as well as the high-spin levels, by the modification of the Hamiltonian introduced in Sec. II B, its basic trend is already seen without the modification. Thus, the $V_{\rm MU}$ interaction gives a reasonable evolution of the $\nu 0g_{9/2}$ orbit, if the $9/2_1^+$ levels are of single-particle origin. Besides Cr and Fe isotopes, the present calculation also reproduces the systematics of $9/2_1^+$ in Ni isotopes. This shows wide applicability of the present Hamiltonian in this mass region.

The single-particle properties of odd-mass Cr, Fe, and Ni isotopes are probed from the spectroscopic factors for neutron transfer reactions. The measured spectroscopic factors are compared to the calculated values in Table I. While the experimental values scatter in some nuclei, the present calculation well reproduces their systematic behavior: ~ 0.5
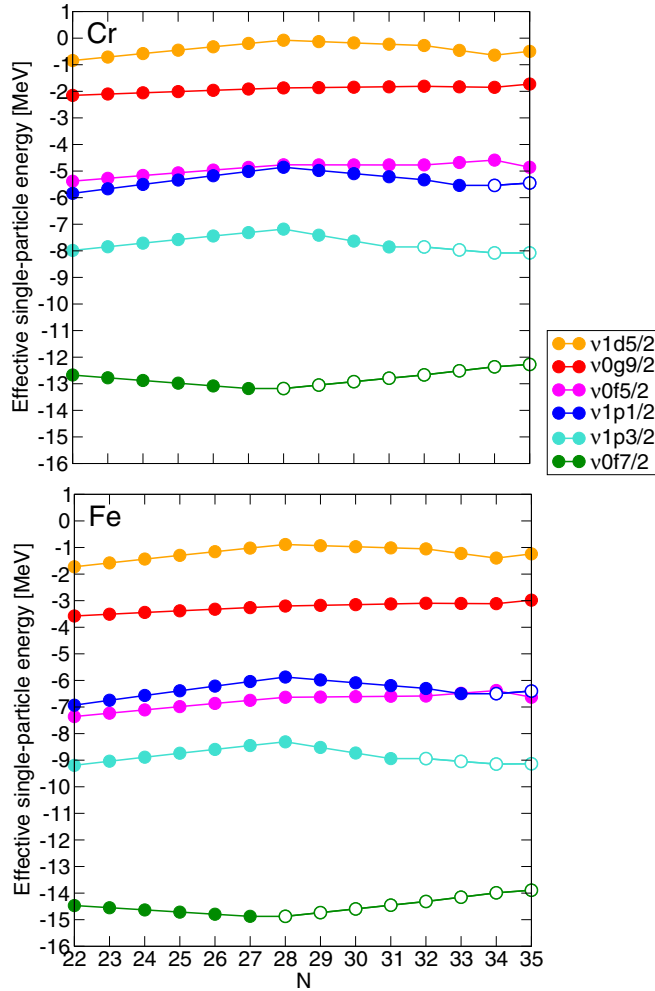
FIG. 9. (Color online) Effective single-particle energies (ESPEs) of a neutron for Cr and Fe isotopes. Open circles represent ESPEs calculated as the hole states to specify the occupied states.

FIG. 10. (Color online) Plots of $-S_n + E_x(9/2_1^+)$. Experimental one-neutron separation energies S_n are taken from [47–49,62–64]. The Coulomb energy is corrected in the calculated S_n according to [9].

for $9/2_1^+$ states and 0.1–0.2 for $5/2_1^+$ states. This indicates that these $9/2_1^+$ states are single-particle-like states but that the $5/2_1^+$ states are not. Hence, the excitation energy of $9/2_1^+$ in these nuclei is influenced directly by the location of the $\nu 0g_{9/2}$ orbit.

Neutron ESPEs [88] in Cr and Fe isotopes are displayed in Fig. 9 using the present Hamiltonian. The ESPEs of $\nu 0g_{9/2}$ are rather constant with increasing neutron number, and so are the shell gaps between the fp shell and $\nu 0g_{9/2}$. This indicates that the evolution of the $9/2_1^+$ level is explained by the Fermi surface approaching the $\nu 0g_{9/2}$ orbit with increasing neutron number. This is in contrast to the result of a previous shell-model study [20] in which this evolution occurs due to the lowering of the $0g_{9/2}$ orbit. This lowering was realized in Ref. [20] by shifting the $T = 1$ monopole interaction between $0p_{3/2}$ and $0g_{9/2}$ by -1.0 MeV. It should be noted that the $T = 1$, $j \neq j'$ monopole matrix elements in realistic interactions are, in general, rather small [43].

The evolution of the $\nu 0g_{9/2}$ orbit can be probed through experimental energies. Namely, in the independent-particle limit, the $\nu 0g_{9/2}$ single-particle energy is identical to the
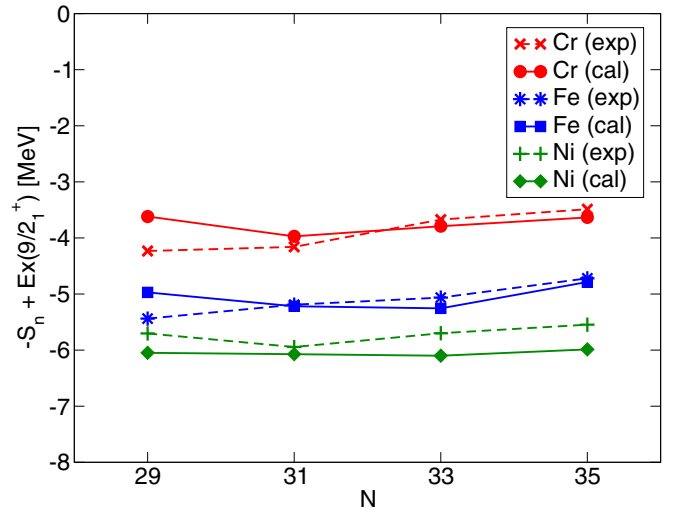
energy of the $9/2_1^+$ state measured from the adjacent even-even core nucleus, $-S_n + E_x(9/2_1^+)$. This idea can be extended to deformed single-particle energies. In Fig. 10, the $-S_n + E_x(9/2_1^+)$ values are compared between the experimental data and the present calculation. The observed stabilities in $-S_n + E_x(9/2_1^+)$ along the Cr, Fe, and Ni isotopic chains suggest that the $\nu 0g_{9/2}$ single-particle energies are kept nearly constant as shown in Fig. 9.

V. CONCLUSIONS

We have investigated unnatural-parity high-spin states in neutron-rich Cr and Fe isotopes by large-scale shell-model calculations for the model space of fp-shell $+ 0g_{9/2} + 1d_{5/2}$ orbits with the truncation allowing $1\hbar\omega$ excitation of a neutron. The effective Hamiltonian is composed of GXPF1Br for fp-shell orbits and a modified V_{MU} for the other parts. The shell-model calculations with the present Hamiltonian can describe and predict the energy levels of both natural- and unnatural-parity states up to the high-spin states in Cr and Fe isotopes with $N \leqslant 35$. This shell-model calculation has shown that the $9/2_1^+$ states are the lowest positive-parity states in these odd-mass nuclei and the level spacings of the bands built on $9/2_1^+$ in odd-mass A nuclei are similar to those of the 0_1^+ bands in the neighboring even-mass $A - 1$ nuclei.

We have also discussed the deformations of Cr and Fe isotopes by utilizing the Q-constrained Hartree-Fock calculation with variation after parity projection. This study indicates that the present Cr and Fe nuclei have the prolate deformations on the whole. In these energy surfaces, the excitation of one neutron into the $\nu 0g_{9/2}$ orbit plays the role of enhancing the prolate deformation. The electric intrinsic quadrupole moments Q_0, which are calculated using the electric spectroscopic quadrupole moments Q_S and the $B(E2)$ values obtained in the shell-model calculation, support the

prolate deformations of the states in the band built on $9/2_1^+$ in odd-mass Cr and Fe nuclei and indicate that their dominant K quantum number is $1/2$. This situation corresponds to the decoupling limit of the particle-plus-rotor model, which can explain the systematics of the positive-parity level schemes in these Cr and Fe nuclei.

In the present calculation, the ESPEs of $\nu 0g_{9/2}$ in Cr and Fe isotopes are rather constant in the region with $N \leqslant 35$, which means very weak attraction between the fp-shell orbits and the $0g_{9/2}$ orbit as given by V_{MU}. We have shown that this can be confirmed by the one-neutron separation energy (S_n) and the excitation energy of $9/2_1^+ [E_x(9/2_1^+)]$. This result indicates that the sharp drop in the $9/2_1^+$ levels in Cr and Fe nuclei in this mass region is explained by the Fermi surface approaching the $\nu 0g_{9/2}$ orbit with the increase in neutron number. A similar evolution of the $9/2_1^+$ levels in Ni isotopes is also well reproduced with the present calculations, thus confirming this picture.

[1] A. Huck *et al.*, Phys. Rev. C **31**, 2226 (1985).
[2] A. Gade *et al.*, Phys. Rev. C **74**, 021302(R) (2006).
[3] R. V. F. Janssens *et al.*, Phys. Lett. B **546**, 55 (2002).
[4] D.-C. Dinca *et al.*, Phys. Rev. C **71**, 041302(R) (2005).
[5] R. Chapman *et al.*, Nucl. Phys. A **119**, 305 (1968).
[6] A. Bürger *et al.*, Phys. Lett. B **622**, 29 (2005).
[7] D. Steppenbeck *et al.*, Nature **502**, 207 (2013).
[8] T. Otsuka, R. Fujimoto, Y. Utsuno, B. A. Brown, M. Honma, and T. Mizusaki, Phys. Rev. Lett. **87**, 082502 (2001).
[9] M. Honma, T. Otsuka, B. A. Brown, and T. Mizusaki, Phys. Rev. C **69**, 034335 (2004).
[10] E. Caurier *et al.*, Rev. Mod. Phys. **77**, 427 (2005).
[11] T. Otsuka, T. Suzuki, R. Fujimoto, H. Grawe, and Y. Akaishi, Phys. Rev. Lett. **95**, 232502 (2005).
[12] R. Broda *et al.*, Phys. Rev. Lett. **74**, 868 (1995).
[13] T. Ishii *et al.*, Phys. Rev. Lett. **84**, 39 (2000).
[14] O. Sorlin *et al.*, Phys. Rev. Lett. **88**, 092501 (2002).
[15] B. Pritychenko *et al.*, At. Data Nucl. Data Tables **98**, 798 (2012).
[16] N. Aoi *et al.*, Phys. Rev. Lett. **102**, 012502 (2009).
[17] T. Baugher *et al.*, Phys. Rev. C **86**, 011305(R) (2012).
[18] H. L. Crawford *et al.*, Phys. Rev. Lett. **110**, 242701 (2013).
[19] W. Rother *et al.*, Phys. Rev. Lett. **106**, 022502 (2011).
[20] K. Kaneko, Y. Sun, M. Hasegawa, and T. Mizusaki, Phys. Rev. C **78**, 064312 (2008).
[21] H. Oba and M. Matsuo, Prog. Theor. Phys. **120**, 143 (2008).
[22] S. M. Lenzi, F. Nowacki, A. Poves, and K. Sieja, Phys. Rev. C **82**, 054301 (2010).
[23] A. Gade *et al.*, Phys. Rev. Lett. **112**, 112503 (2014).
[24] E. K. Warburton, J. A. Becker, and B. A. Brown, Phys. Rev. C **41**, 1147 (1990).
[25] Y. Utsuno, T. Otsuka, T. Mizusaki, and M. Honma, Phys. Rev. C **60**, 054315 (1999).
[26] Y. Tsunoda, T. Otsuka, N. Shimizu, M. Honma, and Y. Utsuno, Phys. Rev. C **89**, 031301(R) (2014).
[27] D. E. Appelbe *et al.*, Phys. Rev. C **67**, 034309 (2003).
[28] A. N. Deacon *et al.*, Phys. Lett. B **622**, 151 (2005).
[29] S. J. Freeman *et al.*, Phys. Rev. C **69**, 064301 (2004).
[30] A. N. Deacon *et al.*, Phys. Rev. C **76**, 054303 (2007).
[31] N. Hoteling *et al.*, Phys. Rev. C **77**, 044314 (2008).
[32] A. N. Deacon *et al.*, Phys. Rev. C **83**, 064305 (2011).

[33] G. A. Lalazissis *et al.*, Nucl. Phys. A **628**, 221 (1998).
[34] Y.-C. Yang *et al.*, Phys. Lett. B **700**, 44 (2011).
[35] I. Matea *et al.*, Phys. Rev. Lett. **93**, 142503 (2004).
[36] N. Vermeulen *et al.*, Phys. Rev. C **75**, 051302(R) (2007).
[37] A. P. Zuker, J. Retamosa, A. Poves, and E. Caurier, Phys. Rev. C **52**, R1741 (1995).
[38] D. H. Gloeckner and R. D. Lawson, Phys. Lett. **53B**, 313 (1974).
[39] T. Mizusaki, N. Shimizu, Y. Utsuno, and M. Honma (private communication).
[40] N. Shimizu, arXiv:1310.5431.
[41] M. Honma, T. Otsuka, B. A. Brown, and T. Mizusaki, Eur. Phys. J. A **25**, 499 (2005).
[42] M. Honma *et al.*, RIKEN Accel. Prog. Rep. **41**, 32 (2008).
[43] T. Otsuka, T. Suzuki, M. Honma, Y. Utsuno, N. Tsunoda, K. Tsukiyama, and M. Hjorth-Jensen, Phys. Rev. Lett. **104**, 012501 (2010).
[44] Y. Utsuno, T. Otsuka, B. A. Brown, M. Honma, T. Mizusaki, and N. Shimizu, Phys. Rev. C **86**, 051301(R) (2012).
[45] G. Bertsch *et al.*, Nucl. Phys. A **284**, 399 (1977).
[46] B. A. Brown *et al.*, Ann. Phys. **182**, 191 (1988).
[47] H. Junde, Nucl. Data Sheets **109**, 787 (2008), and references therein .
[48] M. R. Bhat, Nucl. Data Sheets **85**, 415 (1998), and references therein .
[49] C. M. Baglin, Nucl. Data Sheets **95**, 215 (2002), and references therein .
[50] A. Bohr and B. R. Mottelson, *Nuclear Structure, Vol. II: Nuclear Deformations* (W. A. Benjamin, Reading, MA, 1975).
[51] S. Zhu *et al.*, Phys. Rev. C **74**, 064315 (2006).
[52] D. Steppenbeck *et al.*, Phys. Rev. C **85**, 044316 (2012).
[53] H. Junde *et al.*, Nucl. Data Sheets **112**, 1513 (2011), and references therein .
[54] C. D. Nesaraja *et al.*, Nucl. Data Sheets **111**, 897 (2010), and references therein .
[55] E. Browne and J. K. Tuli, Nucl. Data Sheets **114**, 1849 (2013), and references therein .
[56] Y. Sun, Y. C. Yang, H. L. Liu, K. Kaneko, M. Hasegawa, and T. Mizusaki, Phys. Rev. C **80**, 054306 (2009).
[57] P. Ring and P. Schuck, *The Nuclear Many-Body Problem* (Springer-Verlag, Berlin, 1980).

[58] F. S. Stephens, Rev. Mod. Phys. **47**, 43 (1975).

[59] T. Mizusaki, T. Otsuka, Y. Utsuno, M. Honma, and T. Sebe, Phys. Rev. C **59**, R1846 (1999).

[60] N. Shimizu, Y. Utsuno, T. Mizusaki, M. Honma, Y. Tsunoda, and T. Otsuka, Phys. Rev. C **85**, 054301 (2012).

[61] S. Cavallaro *et al.*, Nucl. Phys. A **293**, 125 (1977).

[62] H. Junde, Nucl. Data Sheets **110**, 2689 (2009), and references therein .

[63] M. R. Bhat, Nucl. Data Sheets **88**, 417 (1999), and references therein .

[64] B. Erjun and H. Junde, Nucl. Data Sheets **92**, 147 (2001), and references therein .

[65] M. N. Rao *et al.*, Nucl. Phys. A **121**, 1 (1968).

[66] R. Bock *et al.*, Nucl. Phys. **72**, 273 (1965).

[67] D. C. Kocher and W. Haeberli, Nucl. Phys. A **196**, 225 (1972).

[68] A. E. Macgregor and G. Brown, Nucl. Phys. A **198**, 237 (1972).

[69] R. H. Fulmer and A. L. McCarthy, Phys. Rev. **131**, 2133 (1963).

[70] J. R. Maxwell and W. C. Parkinson, Phys. Rev. **135**, B82 (1964).

[71] H. M. Sen Gupta *et al.*, Nucl. Phys. A **160**, 529 (1971).

[72] J. A. Thomson, Nucl. Phys. A **227**, 485 (1974).

[73] K. C. McLean *et al.*, Nucl. Phys. A **191**, 417 (1972).

[74] T. Taylor and J. A. Cameron, Nucl. Phys. A **337**, 389 (1980).

[75] M. S. Chowdhury and H. M. Sen Gupta, Nucl. Phys. A **205**, 454 (1973).

[76] J. A. Aymar *et al.*, Nucl. Phys. A **207**, 596 (1973).

[77] O. Iwamoto *et al.*, Nucl. Phys. A **576**, 387 (1994).

[78] B. L. Cohen *et al.*, Phys. Rev. **126**, 698 (1962).

[79] R. H. Fulmer *et al.*, Phys. Rev. **133**, B955 (1964).

[80] E. R. Cosman *et al.*, Phys. Rev. **163**, 1134 (1967).

[81] J. A. Aymar *et al.*, Nucl. Phys. A **213**, 125 (1973).

[82] I. M. Turkiewicz *et al.*, Nucl. Phys. A **143**, 641 (1970).

[83] T. R. Anfinsen *et al.*, Nucl. Phys. A **157**, 561 (1970).

[84] G. A. Huttlin *et al.*, Nucl. Phys. A **227**, 389 (1974).

[85] P. Roussel *et al.*, Nucl. Phys. A **155**, 306 (1970).

[86] O. Karban *et al.*, Nucl. Phys. A **535**, 377 (1991).

[87] F. Videbaek *et al.*, Nucl. Phys. A **433**, 441 (1985).

[88] M. H. Storm *et al.*, J. Phys. G: Nucl. Phys. **9**, L165 (1983).